HHS Public Access

Author manuscript

J Vasc Interv Radiol. Author manuscript; available in PMC 2022 July 29.

Published in final edited form as:

J Vasc Interv Radiol. 2022 July ; 33(7): 814–824.e3. doi:10.1016/j.jvir.2022.04.006.

MR Imaging Biomarkers for the Prediction of Outcome after Radiofrequency Ablation of Hepatocellular Carcinoma: Qualitative and Quantitative Assessments of the Liver Imaging Reporting and Data System and Radiomic Features

Alexandra Petukhova-Greenstein, BSc,

Tal Zeevi, MS,

Junlin Yang, MS,

Nathan Chai, MD,

Paul DiDomenico, MD, MBA, MS,

Yanhong Deng, MPH,

Maria Ciarleglio, PhD,

Stefan P. Haider, MD,

Ifeyinwa Onyiuke, MD,

Rohil Malpani, MD,

MingDe Lin, PhD,

Ahmet S. Kucukkaya, BSc,

Luzie A. Gottwald, BSc,

Bernhard Gebauer, MD,

Margarita Revzin, MD, MS,

John Onofrey, PhD,

Lawrence Staib, PhD,

Gowthaman Gunabushanam, MD,

Tamar Taddei, MD,

Julius Chapiro, MD, PhD

Department of Radiology and Biomedical Imaging (A.P.-G., T.Z., N.C., P.D., S.P.H., R.M., M.L., A.K., L.A.G., M.R., J.O., L.S., G.G., J.C.), Yale School of Medicine, New Haven, Connecticut; Charité Universitätsmedizin Berlin (A.P.-G., A.K., L.A.G., B.G.), Corporate Member of Freie Universität Berlin, Humboldt-Universität, and Berlin Institute of Health, Institute of Radiology, Berlin, Germany; Department of Biomedical Engineering (J.Y., L.S.), Yale School of Engineering and Applied Science, New Haven, Connecticut; Visage Imaging, Inc. (M.L.), San Diego,

Address correspondence to J.C., Department of Radiology and Biomedical Imaging, Yale University School of Medicine, 300 Cedar Street New Haven, CT 06520; julius.chapiro@yale.edu; Twitter handle: @JuliusChapiro.

T.T. and J.C. contributed equally to this work and are co-first authors.

From the 2020 Radiological Society of North America Annual Meeting, RSNA, Abstract No. 20009949, “Qualitative and Quantitative Assessment of Diagnostic LI-RADS Features for Prediction of Outcome in Nodular Hepatocellular Carcinoma.”

Figure E1 and Appendix A can be found by accessing the online version of this article on www.jvir.org and selecting the Supplemental Material tab.

California; VA Connecticut Healthcare System (P.D., I.O., G.G, T.T.), West Haven, Connecticut; Department of Biostatistics (Y.D., M.C.), Yale University School of Public Health, New Haven, Connecticut; Department of Internal Medicine (T.T.), Section of Digestive Diseases, Yale School of Medicine, New Haven, Connecticut; [8] Department of Urology (J.O.), Yale School of Medicine, New Haven, Connecticut.

Abstract

Purpose: To assess the Liver Imaging Reporting and Data System (LI-RADS) and radiomic features in pretreatment magnetic resonance (MR) imaging for predicting progression-free survival (PFS) in patients with nodular hepatocellular carcinoma (HCC) treated with radiofrequency (RF) ablation.

Material and Methods: Sixty-five therapy-naïve patients with 85 nodular HCC tumors <5 cm in size were included in this Health Insurance Portability and Accountability Act–compliant, institutional review board–approved, retrospective study. All patients underwent RF ablation as first-line treatment and demonstrated complete response on the first follow-up imaging. Gadolinium-enhanced MR imaging biomarkers were analyzed for LI-RADS features by 2 board-certified radiologists or by analysis of nodular and perinodular radiomic features from 3-dimensional segmentations. A radiomic signature was calculated with the most informative features of a least absolute shrinkage and selection operator Cox regression model using leave-one-out cross-validation. The association between both LI-RADS features and radiomic signatures with PFS was assessed via the Kaplan-Meier analysis and a weighted log-rank test.

Results: The median PFS was 19 months (95% confidence interval, 16.1–19.4) for a follow-up period of 24 months. Multifocality ($P = .033$); the appearance of capsular continuity, compared with an absent or discontinuous capsule ($P = .012$); and a higher radiomic signature based on nodular and perinodular features ($P = .030$) were associated with poorer PFS in early-stage HCC. The observation size, presence of arterial hyperenhancement, nonperipheral washout, and appearance of an enhancing “capsule” were not associated with PFS ($P > .05$).

Conclusions: Although multifocal HCC clearly indicates a more aggressive phenotype even in early-stage disease, the continuity of an enhancing capsule and a higher radiomic signature may add value as MR imaging biomarkers for poor PFS in HCC treated with RF ablation.

Hepatocellular carcinoma (HCC) can be treated with curative intent using image-guided radiofrequency (RF) ablation (1,2). Although RF ablation is a safe and effective first-line treatment, recurrence and outcome prediction remain a challenge because of the heterogeneity in both the clinical background and imaging characteristics of HCC (3). The Liver Imaging Reporting and Data System (LI-RADS) algorithm involves stratifying multiphase imaging criteria to report characteristic alterations, such as arterial hypervascularity with reduced or absent portal venous supply, and helps diagnose HCC in a standardized manner (4–6). Radiomics, on the other hand, has added incremental value to the field of standardized medical image analysis as well as quantification of phenotypic differences that are not visibly evident (7,8). This technology enables the detection of imaging features by applying image characterization algorithms and quantifying tumor characteristics, such as image intensity, shape, and texture (9,10).

The risk of disease progression after ablation is related to the characteristics of the tumor at the time of treatment, such as multifocality, size, and the degree of differentiation (11). There are biological and technical barriers to the standardized assessment of tumor differentiation, such as heterogeneity of intratumoral and peritumoral microenvironments and variability of imaging techniques and contrast agents (12).

This study aimed to identify pretreatment magnetic resonance (MR) imaging biomarkers to predict progression-free survival (PFS) by gaining insight into the imaging representation of the biological continuum of nodular HCC through qualitative and quantitative assessments of characteristic LI-RADS, radiomic, and additional auxiliary features in patients treated with RF ablation.

MATERIALS AND METHODS

Patients

This observational, Health Insurance Portability and Accountability Act of 1996–compliant, retrospective study assessed therapy-naive patients who underwent RF ablation for newly diagnosed HCC between 2003 and 2018. The Yale University Institutional Review Board and the West Haven VA Institutional Reveiw Board approved the protocol and waived the requirement for informed consent. Tumor board consensus on treatment allocation was based on individual consideration of each patient, including parameters such as size, location, liver function, relevant comorbidities, and performance status.

This study included patients with the following: (*a*) a new diagnosis of HCC based on either imaging criteria consistent with international guidelines, histologic assessment of a radiologically indeterminate tumor, or consensus of the tumor board; (*b*) RF ablation as the first-line therapy for HCC; (*c*) the presence of pretreatment contrast-enhanced multiphase MR imaging with an extracellular agent; (*d*) nodular HCC within the Milan criteria (Appendix A, available online on the article's Supplemental Material page at www.jvir.org) (13); (*e*) complete ablation after the treatment cycle based on the first follow-up imaging (ie, no evidence of a residual unablated tumor); and (*f*) no concomitant malignancies. This study excluded patients with the following: (*a*) insufficient quality of imaging (Appendix A, available online at www.jvir.org), (*b*) nodular tumors with satellite nodules or peritumoral arterial enhancement or infiltrative growth pattern of HCC, and (*c*) combined treatment modalities. The flowchart of patient selection is illustrated in Figure 1.

Patient Characteristics

A total of 65 patients fulfilled the inclusion criteria. The mean age was 62.5 years ± 8.2, and 57 (87.7%) patients were men. The primary disease etiologies were hepatitis C virus (n = 27, 41.5%), alcoholic liver disease (n = 8, 12.3%), and a combination of hepatitis C virus and alcoholic liver disease (n = 17, 26.2%). Barcelona Clinic Liver Cancer (BCLC) stages were BCLC 0 (n = 20, 30.8%) and BCLC A (n = 45, 69.2%). The Child-Pugh (CP) scores were CP A (n = 45, 69.2%) and CP B (n = 20, 30.8%). Baseline clinical characteristics are shown in Table 1. To assess synthetic liver function and other liver disease–related conditions, a laboratory profile was analyzed (Appendix A, available online at www.jvir.org).

Qualitative and Quantitative Assessments of the LI-RADS Features

All MR imaging studies were performed using 1.5 and 3 Tesla Siemens MR imaging scanners (Siemens Medical Solutions, Erlangen, Germany) with multichannel phased-array coils. Image acquisition included the following phases: (*a*) precontrast, (*b*) arterial, (*c*) portal venous, and (*d*) delayed phases. MR imaging features were analyzed independently by 2 experienced board-certified and fellowship-trained radiologists who were blinded to clinical features and outcome (P.D., with 11 years of experience, and I.O., with 23 years of experience). Further details are described in Appendix A (available online at www.jvir.org). The analysis included the number of tumors and the following LI-RADS criteria for the dominant tumor: (*a*) observation size, (*b*) arterial phase hyperenhancement (APHE), (*c*) nonperipheral "washout," and (*d*) appearance of an enhancing "capsule" in the portal venous or delayed phase (Fig 2). APHE was designated as either homogeneous or heterogeneous. The appearance of an enhancing "capsule" was characterized as either continuous (smooth) or discontinuous (either smooth or nonsmooth).

Image Preprocessing for Radiomic Analysis and Feature Extraction

For radiomic feature extraction in multiphase MR imaging, a multistep image preprocessing workflow was established (Fig 3). Further steps of the preprocessing process are presented in Appendix A (available online at www.jvir.org). Regarding the 3-dimensional tumor segmentation, dominant tumors were predefined in the LI-RADS analysis by 2 radiologists (P.D. and I.O.) and subsequently segmented semiautomatically with IntelliSpace Portal V8 (Philips Healthcare, Cambridge, Massachusetts). To include the whole tumor volume, the segmentations were performed in the phase with the largest tumor volume visible. Further, the segmentation was simultaneously compared with the tumor appearance in the remaining MR imaging phases. All 3-dimensional segmentations were reviewed and adjusted by a radiologist (M.R., with 11 years of experience). To capture the radiomic features from the perinodular area, a peripheral ring was created by shrinking the tumor boundaries by 30% in diameter in MATLAB 9.7 (MathWorks Inc., Natick, Massachusetts). The radiomic features were extracted using PyRadiomics 3.0 in Python 3.8.0 (14,15).

RF Ablation Procedure

RF ablation was performed under ultrasound and/or computed tomography (CT) guidance by 2 fellowship-trained interventional radiologists (G.G.) with 32 and 13 years of experience, respectively. LeVeen (Boston Scientific, Marlborough, Massachusetts) or Covidien Cool-tip (Medtronic, Dublin, Ireland) probes were used under image guidance. A subset of patients underwent laparoscopic RF ablation if this approach was recommended by the tumor board, and these procedures were performed by 2 surgical oncologists with over 5 and 15 years of experience. On the basis of contrast-enhanced CT or the comparison with pretreatment CT, the attending physician determined intraprocedurally the appropriate ablation margins and whether any significant bleeding was present. Alternatively, during an ultrasound-guided RF ablation procedure, an appropriate ring of hypodensity surrounding the ablated lesion was used as a treatment endpoint.

Statistical Analysis

PFS was defined as the time from the day of the RF ablation treatment to the first day of either disease progression (Appendix A, available online at www.jvir.org) or death by any cause. Survival times were analyzed using the log-rank test for comparison among treatment groups and estimated using the Kaplan-Meier method within the first 24 months and for the whole follow-up period. Because recurrence is 6.5 more likely to be noted in the first year than in the second and because a weighted log-rank test is more sensitive to early differences between survivals, an additional weighted log-rank test was performed using the Gehan-Breslow-Wilcoxon test (16). The details on the definition of the follow-up period are presented in Appendix A (available online at www.jvir.org). Interobserver agreement was compared using the Cohen kappa coefficient (κ) (Appendix A, available online at www.jvir.org) (17). The tests for the assessment of patient characteristics are presented in Appendix A (available online at www.jvir.org).

Given the small data set of 65 patients, the radiomic score (Rad-score) was devised using a leave-one-out cross-validation (LOOCV) framework. LOOCV was chosen because it demonstrates the smallest bias and lowest mean square error for studies with a small population (18). Highly correlated features in the training set were excluded using the Pearson correlation coefficient. The remaining features were normalized with z-score normalization. The least absolute shrinkage and selection operator (LASSO) Cox regression was performed to select the most informative radiomic features with nonzero coefficients (19). To calculate the Rad-score, the selected features were combined linearly and weighted by the corresponding coefficient. To obtain a comparable set of Rad-scores, the test patient's Rad-score was standardized using the mean and SD of the training set Rad-scores in each iteration of the LOOCV.

To assess a potential association of the Rad-score with PFS, the standardized Rad-scores of the test patients (n = 65) were assessed using the Kaplan-Meier survival analysis. According to the Rad-score, patients were classified into high-risk or low-risk groups using X-tile (20). The difference in the survival curves of the high-risk and low-risk groups was evaluated using a weighted log-rank test for a follow-up period of 24 months (the G-rho rank test, rho = 1) (19). The proportional hazards assumption for the radiomic model was tested by scaled Schoenfeld residuals (Appendix A, available online at www.jvir.org). To assess the reliability of the final model, a likelihood ratio test, Akaike information criterion, and Bayesian information criterion were performed.

Statistical analysis was performed using R 4.0.2 (R Project, Vienna, Austria), SPSS version 27 (IBM, Armonk, New York), and X-tile 3.6.1 (Yale University School of Medicine, New Haven, Connecticut). The R packages used are described in Appendix A (available online at www.jvir.org). The reported statistical significance levels were all 2-sided, with the statistical significance level set at .05.

RESULTS

Follow-up and Tumor Progression

For a follow-up period of 24 months, the median PFS of the cohort was 19 months (range, 2–24 months; 95% confidence interval (CI), 16.1–19.4). Additional information for the whole follow-up period is presented in Appendix A (available online at www.jvir.org). The patients were censored at 24 months without an event or liver transplantation. Intrahepatic tumor progression was observed in 26 (40%) patients, whereas no patients experienced progression in the extrahepatic areas. Local tumor progression was observed in 9 (13.8%) patients. However, 1 patient experienced local tumor progression as well as intrahepatic distant recurrence progression. For patients with sufficient follow-up time, 10 of 63 patients demonstrated progression by 12 months, and 26 of 54 patients demonstrated progression by 24 months. The median time interval between pretreatment MR imaging and RF ablation was 51 days (interquartile range [IQR], 29–76 days), with time range of 2–252 days.

Predictive Imaging and Clinical Features

Patients had either 1 (n = 49, 75.4%), 2 (n = 12, 18.5 %), or 3 (n = 4, 6.2%) tumors. The median sizes of the first, second, and third tumors were 2.0 cm (IQR, 1.5–2.5 cm), 1.25 cm (IQR, 1.1–1.6 cm), and 0.95 cm (IQR, 0.8–1.3 cm), respectively. All imaging features, characteristics, median PFS times, and 1-year and 2-year PFS rates are presented in Table 2 and Appendix A (available online at www.jvir.org).

Interobserver agreement was good for an observation size of ≥2 cm (κ = .747), the presence of APHE (κ = .681), and the presence of an enhancing “capsule” (κ = .693). Interobserver agreement was fair for nonperipheral “washout” (κ = .327) and moderate for the continuity of the enhancing “capsule” (κ = .520) and the heterogeneity of APHE (κ = .438).

Multifocality was associated with PFS (χ^2 = 6.8, P = .033). However, the major LI-RADS criteria of an observation size of ≥2 cm (χ^2 = 0.1, P = .75), the presence of APHE (χ^2 = 0.3, P = .59), the homogeneity of APHE (P = 0.60), and nonperipheral “washout” (χ^2 = 0.01, P = .92) demonstrated no association with PFS. The appearance of an enhancing “capsule” showed a trend toward a shorter PFS time, but this was not statistically significant (χ^2 = 3.4, P = .06). Interestingly, the continuity/integrity of the enhancing capsule appearance was associated with poorer PFS. The integrity of an enhancing capsule was classified as the absence, discontinuity, or continuity of a capsule appearance in the portal venous or delayed phase (χ^2 = 8.9, P = .012). The corresponding Kaplan-Meier curves are presented in Figure 4a–d. The PFS analysis for the whole follow-up period is presented in Appendix A (available online at www.jvir.org).

The standard log-rank test for the prediction of PFS during the whole follow-up period demonstrated the following associations: (*a*) multifocality (P = .025), (*b*) a tumor size of ≥2 cm (P = .65), (*c*) the presence of APHE (P = .79), (*d*) the homogeneity of APHE (P = .86), (*e*) nonperipheral “washout” (P = .85), (*f*) the appearance of an enhancing “capsule” (P = .06), and (*g*) the continuity of the enhancing “capsule” in the portal venous or delayed phase (P = .041). Figure 5 shows the examples of patients with different types of an enhancing “capsule.”

For each phase, 107 radiomic features were selected, leading to a total of 856 nodular and perinodular features in the precontrast, arterial, portal venous, and delayed phases (856 PyRadiomics features = 107 features × 2 types of segmentation × 4 MR imaging phases). All radiomic features were subdivided into 7 classes (Appendix A, available online at www.jvir.org).

LASSO Cox regression using LOOCV identified a set of nodular and perinodular radiomic features. The most frequently selected features are presented in Figure 6. Ten nodular and 3 perinodular radiomic features were selected in more than half of the rounds (folds) of the LOOCV. Regarding the nodular radiomic features, 4 features were selected in the delayed phase, 3 in the arterial phase, 2 in the portal venous phase, and 1 in the precontrast phase. The class with the highest number of selected features was the gray-level size zone, a class for the quantification of the connected voxels that share the same gray-level intensity. The most frequently selected nodular feature was the "major axis length," a feature that yields the largest axis lengths of the region of interest. A more detailed description of the most consistent radiomic features that were selected by the LASSO Cox regression is presented in Appendix A (available online at www.jvir.org).

The 3 perinodular features were as follows: (*a*) a first-order statistics feature "Kurtosis" in the precontrast phase, (*b*) a neighboring gray tone difference matrix "Contrast" in the portal venous phase, and (*c*) a shape feature "Sphericity" in the delayed phase.

The validity of proportional hazards assumption for the radiomic model was verified by a Schoenfeld residual plot (Fig E1, Appendix A, available online at www.jvir.org). The likelihood ratio test as a model fit measure for the final model was not significant at the conventional threshold of 0.05 ($P = .066$; Akaike information criterion, 204.24; Bayesian information criterion, 205.54). Normalized Rad-scores ranged from −5.05 to 0.58. According to X-tile, −0.55 was identified as the optimal Rad-score cutoff. Patients were stratified into low-risk (<−0.55) and high-risk (≥−0.55) groups. The weighted log-rank test was statistically significant ($P = .030$) (Fig 4).

DISCUSSION

Using a carefully selected patient cohort, this study identified a set of pretreatment contrast-enhanced MR imaging biomarkers to predict PFS in patients with nodular HCC treated with RF ablation. Imaging features such as multifocality, continuity of an enhancing capsule appearance, and a higher radiomic signature based on nodular and perinodular radiomic features in HCC were predictors for poorer PFS within the first 2 years.

The MR imaging appearance of an enhancing "capsule" in the portal venous or delayed phase can be reflected in characteristic pathological findings in HCC, such as peritumoral fibrosis, the presence of prominent sinusoids, or a combination of both (21). A study by Ishigami et al (22) demonstrated the sensitivity and specificity of extracellular contrast agent–enhanced MR imaging in the diagnosis of the histologic fibrous capsule to be 94.0% and 73.2%, respectively. A pathologically detected fibrous tumor capsule is characteristic of a more progressed HCC within the early stage because it is unlikely to

be found in very early or infiltratively growing HCC (23). Regarding its association with survival, encapsulated HCC is known to be associated with a more favorable outcome regarding the overall HCC population. Therefore, it is important to mention that current research supporting this association has variable inclusion criteria and may not be directly comparable with this work because it also includes patients with a larger or more progressed HCC. Some of these studies (24,25) included patients with a great variety of tumor sizes treated by resection or transplantation, another (26) investigated patients with decompensated liver disease, and others (27,28) examined patients treated with modalities such as transarterial embolization. Given the complexity and heterogeneity of HCC, it may be more accurate not to consider encapsulated HCC per se as a predictor of longer versus shorter PFS times but rather to assess this feature in the context of the HCC stage.

Considering studies with inclusion criteria more comparable with this study, such as stage and size, a pathology-based study (29) with 365 patients demonstrated that the presence of a fibrotic capsule is a predictor of poorer overall survival in surgically resected HCC. Moreover, this study was able to demonstrate that larger tumors have a higher likelihood of having a fibrous capsule, illustrating the interdependence between size and a fibrous capsule as a biological continuum.

In a strongly selected cohort, including patients with a tumor size of up to 5 cm and stable liver function, this study demonstrated a poorer prognosis with a continuous capsule than with a discontinuous and absent capsule. Further, it is important not to confuse the discontinuity of a capsule with a nonsmooth margin of a tumor. HCC with a nonsmooth margin is more common in larger, more progressed HCCs that are associated with tumor disruption and, therefore, a worse outcome (30). However, this study focused on small nodular, early-stage HCC without any sign of extranodular growth.

As special expertise is required to classify different subtypes of major LI-RADS features, such as the enhancing “capsule” (5,31), this study added a component of objectivity by computer-aided image analysis. Radiomic features provide an opportunity to apply quantitative imaging algorithms and find personalized biomarkers to optimize clinical management. Crosstalk between tumor cells and the surrounding peritumoral stroma is a key regulator of hepatocarcinogenesis. Consequently, additional perinodular radiomic features may increase the amount of information obtained from MR imaging by corresponding to this tumor-peritumoral interaction (32,33). This study was able to demonstrate that a radiomic signature based on nodular and perinodular radiomic features may be used as additional information for the prediction of PFS in patients with nodular HCC.

This study has limitations. First, it has a retrospective design with a small number of patients that may lead to overfitting in the machine learning model. The model fit measure with the likelihood ratio test of the final model was not statistically significant at the conventional threshold but may show adequacy given the present trend. Future studies involving larger sets of patients and a comparison to other methods are necessary. Second, the interobserver agreement was moderate for the continuity of the enhancing “capsule” and heterogeneity of APHE and fair for nonperipheral “washout.” Despite the comparable results of prior studies on interobserver agreement, the LI-RADS features as PFS predictors need to be

interpreted with caution and require further validation (34,35). Third, the large time interval between pretreatment MR imaging and RF ablation poses a further limitation. Fourth, an additional assessment of the nearest ablation zone as a known predictor of recurrence was not performed and needs to be assessed in validation studies.

One of the strengths of this analysis is the design of the reading study: before the analysis, 2 board-certified and fellowship-trained radiologists (P.D. and I.O.) with >10 years of experience collectively defined the extensions of the LI-RADS features. Additionally, the selection criteria, such as a restricted number, size, nodular appearance, and complete treatment response, led to a carefully selected patient cohort indicating a “clean” HCC phenotype.

The LI-RADS was a milestone in the standardized diagnosis of HCC. However, there is an unmet clinical need for standardized tumor biomarkers for early detection, especially in ablated tumors without pathology (2). Radiographic and radiomic MR imaging features may provide an additional, noninvasive source of information for risk stratification, personalized HCC management, and treatment allocation (36). Accordingly, MR imaging biomarkers may provide further information for tumor board decision making regarding the optimal choice between thermal ablation, surgical resection, or even transcatheter arterial chemoembolization. For instance, surveillance schedules may be optimized in a risk-related, more frequent way to identify subpopulations with more aggressive subtypes of HCC. Predictive tumor biomarkers could minimize delay between recurrence and detection in the 2 years after treatment and could, therefore, lead to better outcomes (16).

Clinical integration of these MR imaging biomarkers requires prospective validation and further training of radiologists to increase interobserver agreement (31). This will provide more profound information regarding the heterogeneity of HCC phenotypes on MR imaging, their association with survival, and their possible contribution to the growing field of precision medicine.

Supplementary Material

Refer to Web version on PubMed Central for supplementary material.

ACKNOWLEDGMENTS

The authors thank Menelaos Konstantinidis for his advice on and support for the statistical analysis.

J.C. reports grant support from the Society of Interventional Oncology, Guerbet Pharmaceuticals, Philips Healthcare, Boston Scientific, Yale Center for Clinical Investigation, and the National Institutes of Health (R01CA206180); reports personal fees from Guerbet Pharmaceuticals, Bayer, AstraZeneca and Philips Healthcare; and reports nonfinancial support from Guerbet Pharmaceuticals outside the submitted work as well as grants from Guerbet Pharmaceuticals during the conduct of the study. A.P.G. receives grants from the Rolf W. Günther Foundation for Radiological Research (Aachen, Germany). M.L. is a current employee and stockholder at Visage Imaging, Inc., is a former employee at Philips Research North America, is a board member of the Tau Beta Pi Engineering Honor Society, and reports grant support from National Institutes of Health (R01CA206180) during the conduct of the study. The other authors have not identified a conflict of interest.

APPENDIX A

DEFINITION OF THE MILAN CRITERIA

A single tumor with a maximum diameter of 5 cm or a maximum of 3 tumors, none >3 cm in diameter, with no major vessel or extrahepatic involvement.

CRITERIA FOR INSUFFICIENT QUALITY OF IMAGING

Magnetic resonance (MR) imaging with significant motion artifact at the level of the analyzed tumors that would lead to the loss of textural clarity and reduced anatomic detail was determined to be insufficient.

PATIENT CHARACTERISTICS

The laboratory profile included the following values: aspartate aminotransferase, alanine aminotransferase, alkaline phosphatase, total bilirubin, albumin, prothrombin, alpha-fetoprotein, platelet count, creatinine, sodium, neutrophil count, and lymphocyte count. Before ablation, all laboratory values were completely obtained in 65 patients, with the exception of 1 alpha-fetoprotein value and 2 lymphocyte and neutrophil count values. Clinical phenotypes were assessed using the following parameters: Child-Pugh score, Barcelona Clinic Liver Cancer stage, presence of cirrhosis based on the background histology of the liver or on imaging, presence of portal hypertension, presence of previous malignancy, and body mass index.

QUALITATIVE AND QUANTITATIVE ASSESSMENTS OF THE LIVER IMAGING REPORTING AND DATA SYSTEM FEATURES

Before image analysis, pretreatment contrast-enhanced MR imaging features were collectively defined by an example set of patients with early-stage hepatocellular carcinoma aiming to achieve the highest consensus possible among all radiologists. The example data set was chosen by the study coordinator (A.P.G.) providing representative examples for every imaging feature.

IMAGE PREPROCESSING FOR RADIOMIC ANALYSIS AND FEATURE EXTRACTION

First, all MR imaging phases were coregistered to the T1 postcontrast arterial phase image using a linear, affine registration with BioImage Suite, version 3.01 (Yale University School of Medicine, New Haven, Connecticut) (1). Second, all images were normalized to 0 mean and 100 SD and resampled at 1 mm per pixel in all 3 planes (2). A fixed bin width of 25 was used for gray-level discretization, as a fixed bin size is reported to be more reliable than a fixed bin number (3).

DISEASE PROGRESSION

Disease progression was defined as local tumor progression, intrahepatic distant recurrence, or extrahepatic recurrence.

FOLLOW-UP PERIOD

The follow-up period started on the day of the radiofrequency ablation treatment of all tumors of 63 patients. Two patients had 2 synchronous tumors, which were ablated at 2 distinct treatment sessions. For these patients, the progression-free survival started after the second appointment.

COHEN KAPPA COEFFICIENT (κ)

A kappa statistic of 0.8–1.0 was considered excellent agreement, 0.6–0.79 was considered good agreement, 0.4–0.59 was considered moderate agreement, 0.2–0.39 was considered fair agreement, and 0–0.19 was considered poor agreement.

Patient Characteristics

The patient characteristics were compared using the Student t-test for normally distributed continuous variables, the Mann-Whitney U test for nonnormally distributed continuous variables, and the chi-square test for categorical variables.

R PACKAGES

Package “ggplot2,” Version 3.3.2

Package, “ggpubr,” Version 0.4.0

Package “caret,” Version 6.0-86

Package “tidyverse,” Version 1.3.0

Package “survminer,” Version 0.4.9

Package “survival,” Version 3.2-7

Package “elasticnet,” Version 1.3

MR IMAGING FEATURES

Survival times were analyzed using a univariate log-rank test for the whole follow-up period. Furthermore, the log-rank test was weighted toward earlier events and by using the Gehan-Breslow-Wilcoxon test. For the whole follow-up period, the median PFS time of the cohort was 19 months (range, 2–78 months; (95% confidence interval, 20.8–29.1).

CLASSES OF RADIOMIC FEATURES

All radiomic features were subdivided into the following 7 classes: (*a*) first-order statistics, (*b*) shape-based (3-dimensional), (*c*) shape-based (2-dimensional), (*d*) gray-level co-occurrence matrix, (*e*) gray-level run length matrix, (*f*) gray-level size zone matrix, (*g*) neighboring gray tone difference matrix, and (*h*) gray-level dependence matrix.

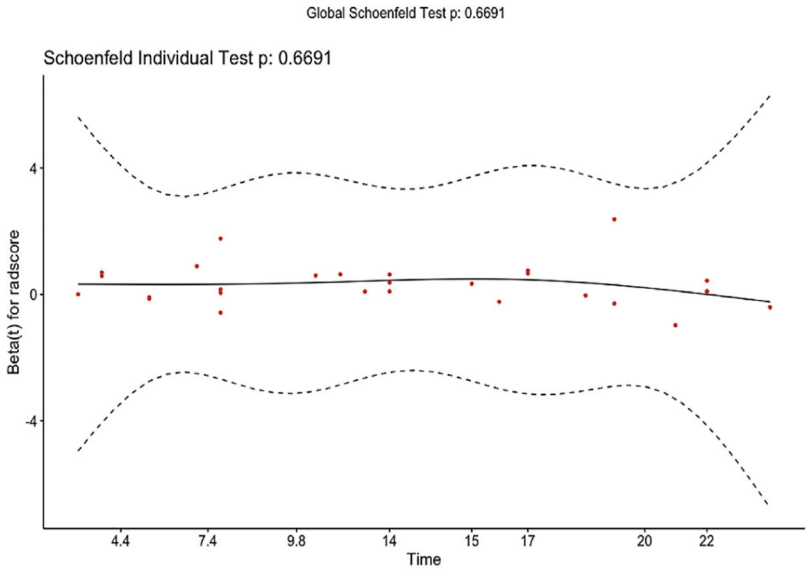

Figure E1.
Schoenfeld residuals. The validity of proportional hazards assumption for the radiomic model was verified by the following Schoenfeld residual plot. To test the proportional hazards assumption for the standardized Rad-scores of the test patients, a Cox proportional hazards model was run ($P = .67$). The proportional hazards assumption is supported by a nonsignificant relationship between residuals and time.

Table E1.

MRI Feature-based PFS Analysis for Entire Follow-Up Period

Imaging feature	Number	Log-rank		Weighted log-rank		Median PFS (95% CI)
		Chi-square	*P* value	Chi-square	*P* value	
Multifocality		10.387	.006	7.862	.020	
1 tumor	49 (75.4%)					22.0 (22.6–32.8)
2 tumors	12 (18.5%)					15.0 (12.2–24.4)
3 tumors	4 (6.2%)					10.5 (0.2–20.8)
Observation size		0.019	.89	0.003	.96	
<2 cm	28 (43.1%)					24.0 (20.4–32.8)
≥2 cm	37 (56.9%)					18.0 (17.9–29.4)
APHE		1.273	.26	0.620	.43	
Absent	6 (9.2%)					27.0 (7.9–39.1)

Imaging feature	Number	Log-rank		Weighted log-rank		Median PFS (95% CI)
		Chi-square	*P* value	Chi-square	*P* value	
Present	59 (90.8%)					19.0 (20.7–29.5)
Heterogeneity of APHE		1.457	.48	1.798	.41	
Absent	6 (9.2%)					27.0 (7.9–39.1)
Homogeneous	30 (46.2%)					21.5 (18.5–32.2)
Heterogeneous	29 (44.6%)					18.0 (18.8–30.7)
Nonperipheral “washout”		0.027	.87	0.037	.85	
Absent	15 (23.1%)					22.0 (16.0–34.7)
Present	50 (76.9%)					19.0 (20.0–29.6)
Enhancing “capsule”		1.883	.17	2.684	.10	
Absent	19 (29.2%)					31.0 (22.7–39.9)
Present	46 (70.8%)					16.5 (17.7–26.9)
Continuity of enhancing “capsule”		2.123	.35	6.325	.042	
Absent	19 (29.2%)					31.0 (22.7–39.9)
Discontinuous	31 (47.7%)					17.0 (17.8–27.5)
Continuous	15 (23.1%)					13.0 (10.4–32.7)

APHE = arterial phase hyperenhancement; CI = confidence interval; PFS = progression-free survival.

Table E2.

Description of Radiomic Features

Radiomic feature	Description
original_shape_MajorAxisLength	This feature yields the largest axis length of the ROI-enclosing ellipsoid and is calculated using the largest principal component λmajor. The principal component analysis is performed using the physical coordinates of the voxel centers defining the ROI. It, therefore, takes spacing into account but does not make use of the shape mesh.
original_firstorder_Kurtosis	Kurtosis is a measure of the “peakedness” of the distribution of values in the image ROI. A higher kurtosis implies that the mass of the distribution is concentrated toward the tail(s) rather than toward the mean. A lower kurtosis implies the reverse: the mass of the distribution is concentrated toward a spike near the mean value.
original_ngtdm_Busyness	A measure of the change from a pixel to its neighbor. A high value for busyness indicates a “busy” image, with rapid changes in intensity between pixels and its neighborhood.
original_glszm_GrayLevelNonUniformity	Measures the similarity of gray-level intensity values in the image, where a lower GLN value correlates with a greater similarity in intensity values.
original_glcm_Correlation	Correlation is a value between 0 (uncorrelated) and 1 (perfectly correlated) showing the linear dependency of gray-level values to their respective voxels in the GLCM.
original_glsz m_Zon eVariance	ZV measures the variance in size volumes for the zones.
original_ngtdm_Contrast	Contrast is a measure of the spatial intensity change but is also dependent on the overall gray-level dynamic range. Contrast is high when both the dynamic range and spatial change rate are high, that is, an image with a large range of gray levels, with large changes between voxels and their neighborhood.
original_shape_Sphericity	Sphericity is a measure of the roundness of the shape of the tumor region relative to a sphere. It is a dimensionless measure, independent of scale and orientation. The value range is 0<sphericity≤1, where a value of 1

Radiomic feature	Description
	indicates a perfect sphere (a sphere has the smallest possible surface area for a given volume, compared with other solids).
original_gldm_DependenceVariance	Measures the variance in dependence size in the image.

GLCM = grey level co-occurrence matrix; GLN = gray level non-uniformity; ROI = region of interest; ZV = zone variance.

ABBREVIATIONS

APHE	arterial phase hyperenhancement
BCLC	Barcelona Clinic Liver Cancer
CI	confidence interval
CP	Child-Pugh
CT	computed tomography
HCC	hepatocellular carcinoma
IQR	interquartile range
LASSO	least absolute shrinkage and selection operator
LI-RADS	Liver Imaging Reporting and Data System
LOOCV	leave-one-out cross-validation
MR	magnetic resonance
PFS	progression-free survival
Rad-score	radiomics score
RF	radiofrequency

REFERENCES

1. Bray F, Ferlay J, Soerjomataram I, Siegel RL, Torre LA, Jemal A. Global cancer statistics 2018: GLOBOCAN estimates of incidence and mortality worldwide for 36 cancers in 185 countries. CA Cancer J Clin 2018; 68: 394–424. [PubMed: 30207593]
2. European Association for the Study of the Liver. EASL clinical practice guidelines: management of hepatocellular carcinoma. J Hepatol 2018; 69:182–236. [PubMed: 29628281]
3. El-Serag HB, Rudolph KL. Hepatocellular carcinoma: epidemiology and molecular carcinogenesis. Gastroenterology 2007; 132:2557–2576. [PubMed: 17570226]
4. Matsui O, Kadoya M, Kameyama T, et al. Benign and malignant nodules in cirrhotic livers: distinction based on blood supply. Radiology 1991; 178:493–497. [PubMed: 1846240]
5. Chernyak V, Fowler KJ, Kamaya A, et al. Liver Imaging Reporting and Data System (LI-RADS) version 2018: imaging of hepatocellular carcinoma in at-risk patients. Radiology 2018; 289:816–830. [PubMed: 30251931]
6. Roberts LR, Sirlin CB, Zaiem F, et al. Imaging for the diagnosis of hepatocellular carcinoma: a systematic review and meta-analysis. Hepatology 2018; 67:401–421. [PubMed: 28859233]

7. Lambin P, Leijenaar RTH, Deist TM, et al. Radiomics: the bridge between medical imaging and personalized medicine. Nat Rev Clin Oncol 2017; 14:749–762. [PubMed: 28975929]
8. Dong J, Qi X. Liver imaging in precision medicine. EBioMedicine 2018; 32:1–2. [PubMed: 29784524]
9. Gillies RJ, Kinahan PE, Hricak H. Radiomics: images are more than pictures, they are data. Radiology 2016; 278:563–577. [PubMed: 26579733]
10. Wu M, Tan H, Gao F, et al. Predicting the grade of hepatocellular carcinoma based on non-contrast-enhanced MRI radiomics signature. Eur Radiol 2019; 29:2802–2811. [PubMed: 30406313]
11. Doyle A, Gorgen A, Muaddi H, et al. Outcomes of radiofrequency ablation as first-line therapy for hepatocellular carcinoma less than 3 cm in potentially transplantable patients. J Hepatol 2019; 70:866–873. [PubMed: 30615906]
12. Paisant A, Vilgrain V, Riou J, et al. Comparison of extracellular and hepatobiliary MR contrast agents for the diagnosis of small HCCs. J Hepatol 2020; 72:937–945. [PubMed: 31870951]
13. Mazzaferro V, Regalia E, Doci R, et al. Liver transplantation for the treatment of small hepatocellular carcinomas in patients with cirrhosis. N Engl J Med 1996; 334:693–699. [PubMed: 8594428]
14. van Griethuysen JJM, Fedorov A, Parmar C, et al. Computational radiomics system to decode the radiographic phenotype. Cancer Res 2017; 77:e104–e107. [PubMed: 29092951]
15. Pyradiomics Documentation Release 3.0 (2020); Available at: https://pyradiomics.readthedocs.io/_/downloads/en/v3.0/pdf/. Accessed February 11, 2022.
16. Boas FE, Do B, Louie JD, et al. Optimal imaging surveillance schedules after liver-directed therapy for hepatocellular carcinoma. J Vasc Interv Radiol 2015; 26:69–73. [PubMed: 25446423]
17. Landis JR, Koch GG. The measurement of observer agreement for categorical data. Biometrics 1977; 33:159–174. [PubMed: 843571]
18. Molinaro AM, Simon R, Pfeiffer RM. Prediction error estimation: a comparison of resampling methods. Bioinformatics 2005; 21:3301–3307. [PubMed: 15905277]
19. Huang Y, Liu Z, He L, et al. Radiomics signature: a potential biomarker for the prediction of disease-free survival in early-stage (I or II) non-small cell lung cancer. Radiology 2016; 281:947–957. [PubMed: 27347764]
20. Camp RL, Dolled-Filhart M, Rimm DL. X-tile: a new bio-informatics tool for biomarker assessment and outcome-based cut-point optimization. Clin Cancer Res 2004; 10:7252–7259. [PubMed: 15534099]
21. Grazioli L, Olivetti L, Fugazzola C, et al. The pseudocapsule in hepatocellular carcinoma: correlation between dynamic MR imaging and pathology. Eur Radiol 1999; 9:62–67. [PubMed: 9933382]
22. Ishigami K, Yoshimitsu K, Nishihara Y, et al. Hepatocellular carcinoma with a pseudocapsule on gadolinium-enhanced MR images: correlation with histopathologic findings. Radiology 2009; 250:435–443. [PubMed: 19095782]
23. Choi JY, Lee JM, Sirlin CB. CT and MR imaging diagnosis and staging of hepatocellular carcinoma: part II. Extracellular agents, hepatobiliary agents, and ancillary imaging features. Radiology 2014; 273:30–50. [PubMed: 25247563]
24. Lu DS, Siripongsakun S, Kyong Lee J, et al. Complete tumor encapsulation on magnetic resonance imaging: a potentially useful imaging biomarker for better survival in solitary large hepatocellular carcinoma. Liver Transpl 2013; 19:283–291. [PubMed: 23280814]
25. Ng IO, Lai EC, Ng MM, Fan ST. Tumor encapsulation in hepatocellular carcinoma. A pathologic study of 189 cases. Cancer 1992; 70: 45–49. [PubMed: 1318778]
26. Franco D, Capussotti L, Smadja C, et al. Resection of hepatocellular carcinomas. Results in 72 European patients with cirrhosis. Gastroenterology 1990; 98:733–738. [PubMed: 2153601]
27. Wakasa K, Sakurai M, Kuroda C, et al. Effect of transcatheter arterial embolization on the boundary architecture of hepatocellular carcinoma. Cancer 1990; 65:913–919. [PubMed: 2153436]
28. Arnaoutakis DJ, Mavros MN, Shen F, et al. Recurrence patterns and prognostic factors in patients with hepatocellular carcinoma in non-cirrhotic liver: a multi-institutional analysis. Ann Surg Oncol 2014; 21: 147–154. [PubMed: 23959056]

29. Iguchi T, Aishima S, Sanefuji K, et al. Both fibrous capsule formation and extracapsular penetration are powerful predictors of poor survival in human hepatocellular carcinoma: a histological assessment of 365 patients in Japan. Ann Surg Oncol 2009; 16:2539–2546. [PubMed: 19533247]

30. Lim JH, Choi D, Park CK, Lee WJ, Lim HK. Encapsulated hepatocellular carcinoma: CT-pathologic correlations. Eur Radiol 2006; 16:2326–2333. [PubMed: 16547706]

31. Davenport MS, Khalatbari S, Liu PS, et al. Repeatability of diagnostic features and scoring systems for hepatocellular carcinoma by using MR imaging. Radiology 2014; 272:132–142. [PubMed: 24555636]

32. Yang JD, Nakamura I, Roberts LR. The tumor microenvironment in hepatocellular carcinoma: current status and therapeutic targets. Semin Cancer Biol 2011; 21:35–43. [PubMed: 20946957]

33. Sun R, Limkin EJ, Vakalopoulou M, et al. A radiomics approach to assess tumour-infiltrating CD8 cells and response to anti-PD-1 or anti-PD-L1 immunotherapy: an imaging biomarker, retrospective multicohort study. Lancet Oncol 2018; 19:1180–1191. [PubMed: 30120041]

34. Barth BK, Donati OF, Fischer MA, et al. Reliability, validity, and reader acceptance of LI-RADS-an in-depth analysis. Acad Radiol 2016; 23: 1145–1153. [PubMed: 27174029]

35. Ehman EC, Behr SC, Umetsu SE, et al. Rate of observation and interobserver agreement for LI-RADS major features at CT and MRI in 184 pathology proven hepatocellular carcinomas. Abdom Radiol (NY) 2016; 41:963–969. [PubMed: 27193793]

36. Shan QY, Hu HT, Feng ST, et al. CT-based peritumoral radiomics signatures to predict early recurrence in hepatocellular carcinoma after curative tumor resection or ablation. Cancer Imaging 2019; 19:11. [PubMed: 30813956]

Appendix References

1. Papademetris X, Jackowski MP, Rajeevan N, et al. BioImage Suite: an integrated medical image analysis suite: an update. Insight J 2006; 2006: 209. [PubMed: 25364771]

2. Collewet G, Strzelecki M, Mariette F. Influence of MRI acquisition protocols and image intensity normalization methods on texture classification. Magn Reson Imaging 2004; 22:81–91. [PubMed: 14972397]

3. Schwier M, van Griethuysen J, Vangel MG, et al. Repeatability of multiparametric prostate MRI radiomics features. Sci Rep 2019; 9: 9441. [PubMed: 31263116]

RESEARCH HIGHLIGHTS

- In this retrospective study of 65 patients with 85 hepatocellular carcinoma (HCC) tumors treated with radiofrequency ablation with complete response on the first follow-up imaging, multifocality was a predictor for worse progression-free survival (PFS).
- The continuity of an enhancing capsule as an extension of the Liver Imaging Reporting and Data System (LI-RADS) was a significant pretreatment magnetic resonance imaging biomarker for worse PFS in early-stage HCC with a size of <5 cm.
- The radiomic-based stratification between the low-risk and high-risk groups included perinodular radiomic features and demonstrated a significant association with PFS.

STUDY DETAILS

Study type: Retrospective, observational, descriptive study

Level of evidence: 4 (SIR-D)

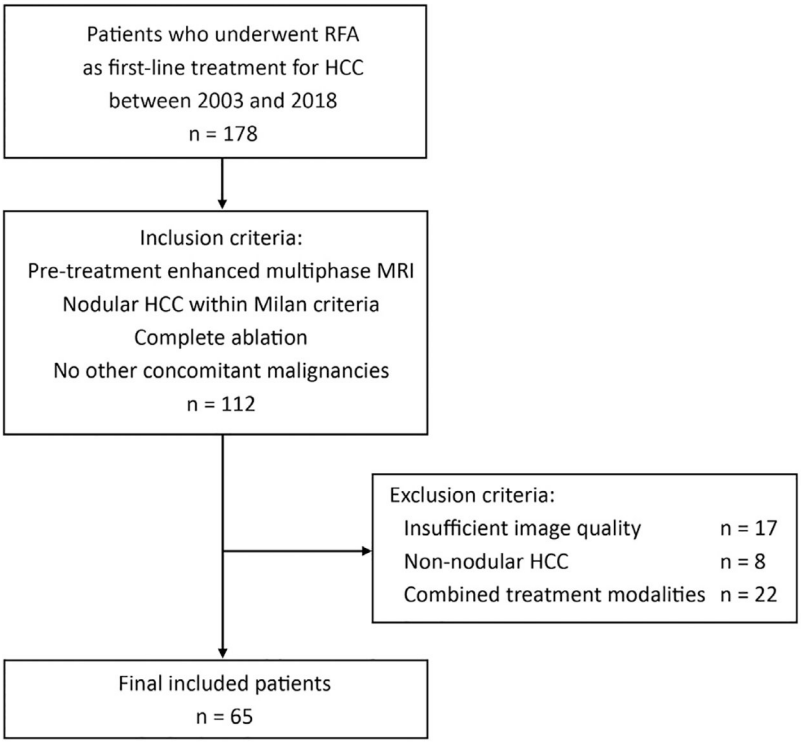

Figure 1.

Flowchart of the eligibility criteria, which illustrates the selection of patients based on the inclusion and exclusion criteria. HCC = hepatocellular carcinoma; MRI = magnetic resonance imaging; RF = radiofrequency.

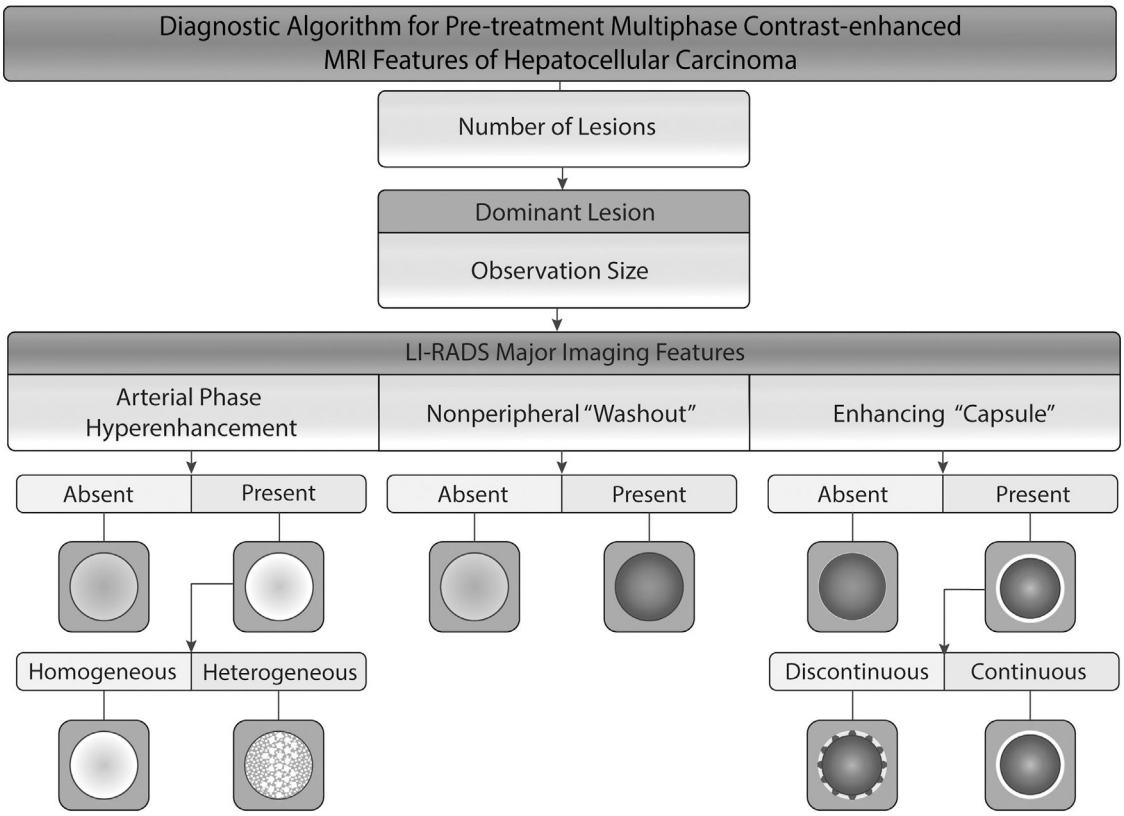

Figure 2.

Diagnostic algorithm for the prospective analysis of imaging features on multiphase magnetic resonance (MR) imaging with an extracellular contrast agent as guidance for 2 board-certified radiologists. Further characterization of the Liver Imaging Reporting and Data System (LI-RADS) features: arterial phase hyperenhancement (APHE) and an enhancing "capsule" had the following strict definitions:

1. APHE was described as homogeneous if there were no elements indicating heterogeneity. Otherwise, it was described as heterogeneous APHE.
2. An enhancing "capsule" was described as continuous if the enhancing rim appeared to be continuous and smooth. The appearance of a discontinuous enhancing capsule was as smooth or nonsmooth.

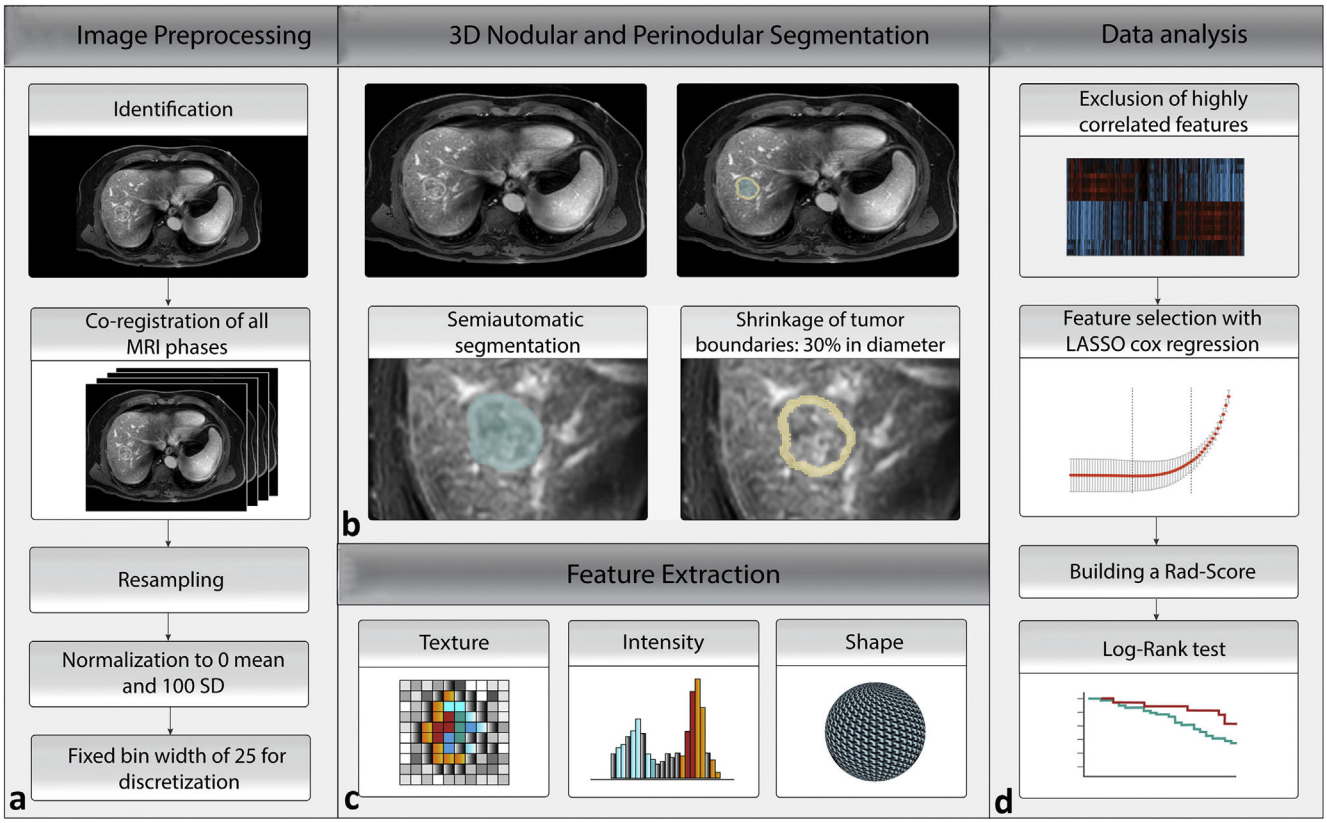

Figure 3.

The radiomics workflow based on a multistep process. **(a)** Preprocessing of multiphase magnetic resonance imaging (MRI). **(b)** Three-dimensional (3D) nodular and perinodular segmentation. **(c)** PyRadiomics feature extraction. **(d)** Data analysis. LASSO = least absolute shrinkage and selection operator; Rad-score = radiomic score.

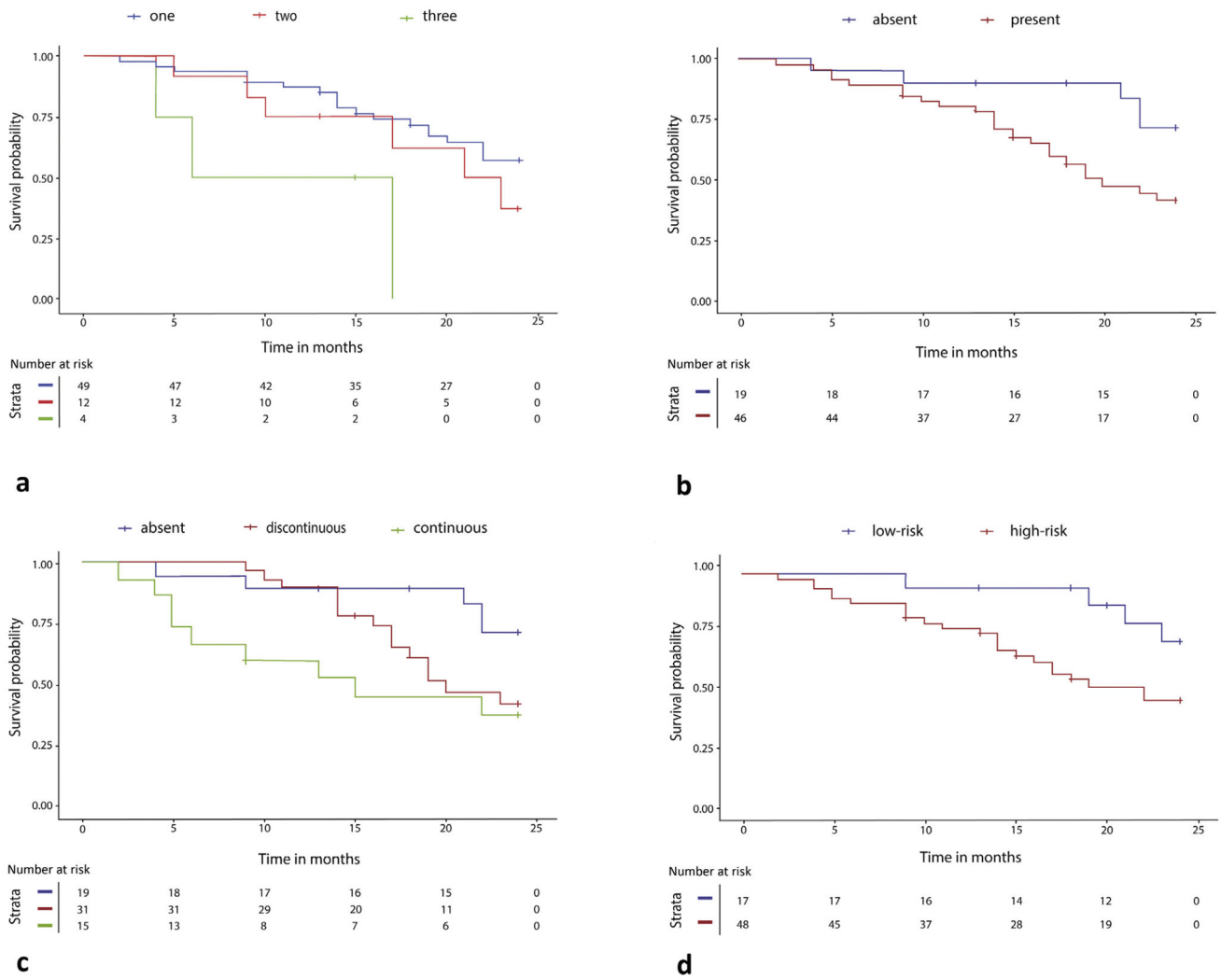

Figure 4.

The graphs demonstrate the results of the Kaplan-Meier survival analyses of radiographic features, analyzed using a weighted log-rank test. **(a)** Multifocality ($P = .033$): patients with 1, 2, and 3 tumors have median progression-free survival (PFS) values of 22.0 (95% confidence interval [CI], 16.8–20.5), 15.0 (95% CI, 12.1–20.6), and 10.5 (95% CI, 0.2–20.8) months, respectively. **(b)** The presence of an enhancing capsule ($P = .06$): patients with an absent and present enhancing "capsule" have median PFS values of 24.0 (95% CI, 18.1–23.7) and 19.0 (95% CI, 16.0–19.7) months, respectively. **(c)** Continuity of the enhancing "capsule" ($P = .012$): patients with an absent, discontinuous, and continuous enhancing "capsule" have median PFS values of 24.0 (95% CI, 18.1–23.7), 17.0 (95% CI, 15.7–19.5), and 13.0 (95% CI, 9.12–18.88) months, respectively. **(d)** The Kaplan-Meier analysis was performed to assess the cumulative survival rates in patients with hepatocellular carcinoma by high-risk and low-risk radiomic signatures ($P = .030$) within the first 2 years of follow-up.

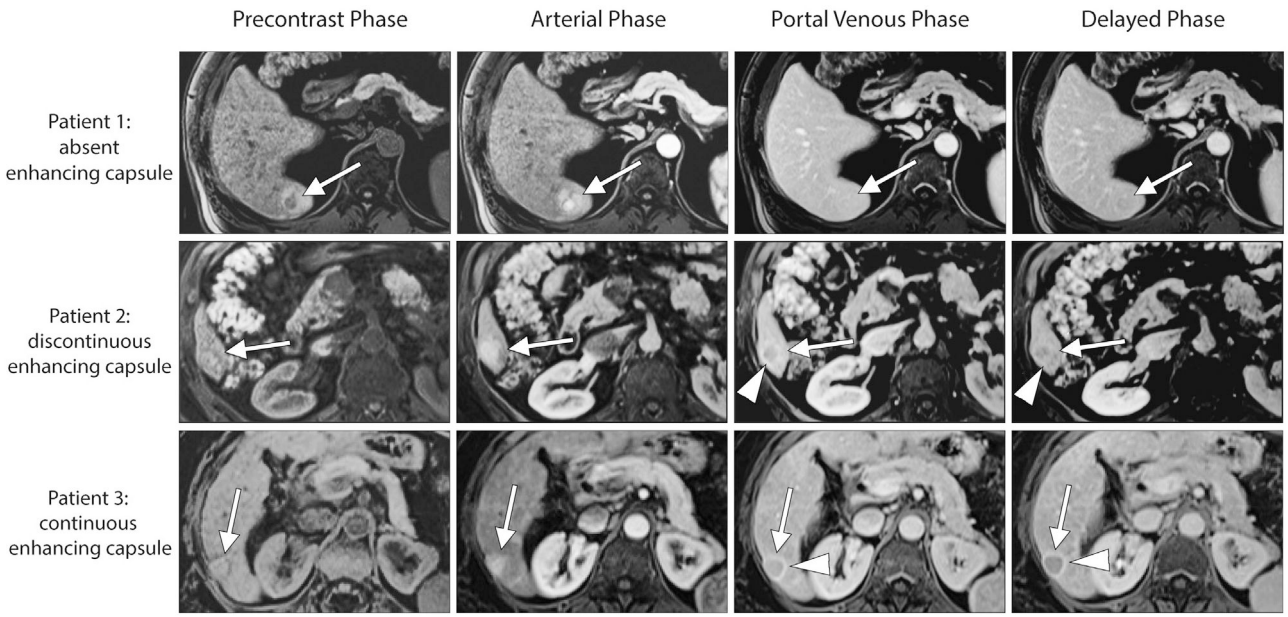

Figure 5.

Axial images were obtained during the unenhanced, arterial, portal venous, and delayed phases on extracellular contrast agent–enhanced magnetic resonance imaging for 3 treatment-naive patients. Patient 1: a 69-year–old male patient with nonalcoholic fatty liver disease and hepatocellular carcinoma (HCC). The 3.1-cm observation (arrow) is characterized by heterogeneous nonrim arterial phase hyperenhancement (APHE), nonperipheral “washout,” and an absent enhancing “capsule” (arrowhead) in the portal venous and delayed phases. Patient 2: a 63-year–old male patient with hepatitis C–related cirrhosis and HCC. The 2.7-cm observation (arrow) is characterized by heterogeneous APHE, nonperipheral “washout,” and a discontinuous “capsule” (arrowhead) in the portal venous and delayed phases. Patient 3: a 64-year–old female patient with hepatitis C–related cirrhosis and HCC. The 2.0-cm observation (arrow) is characterized by heterogeneous APHE, nonperipheral “washout,” and a continuous enhancing “capsule” (arrowhead) in the portal venous and delayed phases. Both readers agreed on the characterization of the listed Liver Imaging Reporting and Data System features in these 3 patients.

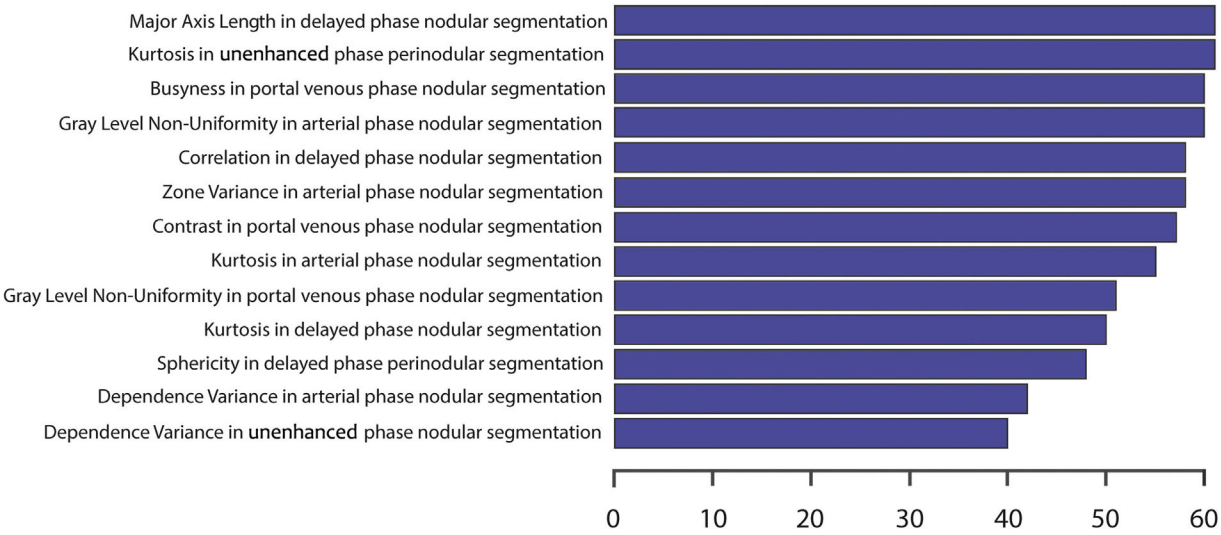

Figure 6.

The horizontal bar plot demonstrates the selected radiomic features by the least absolute shrinkage and selection operator Cox regression in leave-one-out cross-validation. The most consistent features are plotted on the y-axis, and the number of iterations in which the corresponding feature was chosen is plotted on the x-axis.

Table 1.

Demographic and Clinical Characteristics of Patients with Nodular hepatocellular carcinoma

Characteristics	Overall	Progression within the first 2 years		*P* value
	(n = 65)	No (n = 39)	Yes (n = 26)	
Demographics				
Sex, male	57 (87.7%)	33 (84.6%)	24 (92.3%)	.36
Age, y	62.5 (±8.2)	64.0 (±8.4)	60.4 (±7.6)	.13
Ethnicity				.52
White	49 (75.4%)	32 (82.1%)	17 (65.4%)	
Black	11 (16.9%)	5 (12.8%)	6 (23.1%)	
Hispanic	2 (3.1%)	1 (2.6%)	1 (3.8%)	
Other	3 (4.6%)	1 (2.6%)	2 (7.6%)	
Clinical characteristics				
Etiology				.005
HCV and ETOH	17 (26.2%)	6 (15.4%)	11 (42.3%)	
HCV	27 (41.5%)	18 (46.2%)	9 (34.6%)	
ETOH	8 (12.3%)	7 (17.9%)	1 (3.8%)	
NASH	8 (12.3%)	7 (17.9%)	1 (3.8%)	
HBV	1 (1.5%)	1 (2.6%)	0	
Other	4 (6.2%)	0	4 (15.4%)	
BCLC stage				.58
0	20 (30.8%)	11 (28.2%)	9 (34.6%)	
A	45 (69.2%)	28 (71.8%)	17 (65.4%)	
Child-Pugh score				.58
A	45 (69.2%)	26 (66.7%)	19 (73.1%)	
B	20 (30.8%)	13 (33.3%)	7 (26.9%)	
Cirrhosis	58 (89.2%)	38 (97.4%)	20 (76.9%)	.009
Portal hypertension	35 (53.8%)	25 (64.1%)	10 (38.5%)	.042
Previous malignancy	8 (12.3%)	4 (10.3%)	4 (15.4%)	.54
BMI	28.8 (24.5–32.0)	27.7 (24.6–32.3)	27.5 (23.1–31.7)	.50
Laboratory parameters				

J Vasc Interv Radiol. Author manuscript; available in PMC 2022 July 29.

Characteristics	Overall	Progression within the first 2 years		*P* value
	(n = 65)	No (n = 39)	Yes (n = 26)	
AFP (ng/mL)	7.0 (4.0–12.8)	7.7 (4.4–13.0)	7.0 (3.8–15.1)	.46
Total bilirubin (μmol/L)	1.2 (0.7–2.0)	1.2 (0.7–2.0)	1.3 (0.7–1.7)	.95
INR (%)	1.2 (1.1–1.3)	1.1 (1.0–1.3)	1.2 (1.1–1.3)	.47
Albumin (g/L)	3.5 (±0.6)	3.6 (±0.6)	3.6 (±0.6)	.90
Creatinine (μmol/L)	0.9 (0.8–1.0)	0.9 (0.8–1.0)	1.0 (0.8–1.2)	.33
AST (U/L)	55.0 (36.0–84.0)	54.0 (36.0–83.0)	66.0 (37.5–93.0)	.40
ALT (U/L)	49.0 (26.0–83.5)	47.0 (23.0–62.0)	57.5 (33.8–90.5)	.10
Neutrophil (× 10^9/L)	59.3 (±11.8)	59.9 (±11.2)	58.5 (±11.3)	.66
Lymphocyte (× 10^9/L)	24.7 (18.7–34.0)	22.6 (18.7–34.0)	26.5 (19.1–35.2)	.61

Note–Statistical methods included a descriptive assessment of this cohort using the following:

1. Mean (±SD) for normally distributed continuous variables
2. Median (interquartile range) for nondistributed continuous variables
3. Counts (%) for categorical variables.

AFP = alpha-fetoprotein; ALT = alanine aminotransferase; AST = aspartate aminotransferase; BCLC = Barcelona Clinic Liver Cancer; BMI = body mass index; ETOH = ethyl alcohol; HBV = hepatitis B virus; HCV = hepatitis C virus; INR = international normalized ratio; NASH = nonalcoholic steatohepatitis.

Table 2.

Magnetic Resonance Imaging Features

Imaging feature	Number	Log-rank		Weighted log-rank		Median PFS (95% CI)	1-year and 2-year PFS rate
		Chi-square	*P* value	Chi-square	*P* value		
Multifocality		7.410	.025	6.813	.033		
1 tumor	49 (75.4%)					22.0 (16.8–20.5)	41 (83.7%), 23 (46.9%)
2 tumors	12 (18.5%)					15.0 (12.1–20.6)	9 (75.0%), 3 (25.0%)
3 tumors	4 (6.2%)					10.5 (0.2–20.8)	2 (50.0%), 0
Observation size		0.203	.65	0.103	.75		
<2 cm	28 (43.1%)					23.5 (16.1–21.4)	24 (85.7%), 14 (50.0%)
≥2 cm	37 (56.9%)					18.0 (14.8–19.2)	28 (75.7%), 12 (32.4%)
APHE		0.066	.79	0.296	.59		
Absent	6 (9.2%)					21.5 (8.1–26.5)	4 (66.7%), 3 (50.0%)
Present	59 (90.8%)					19.0 (16.1–19.5)	48 (81.4%), 23 (39.0%)
Heterogeneity of APHE		0.293	.86	1.029	.60		
Absent	6 (9.2%)					21.5 (8.1–26.5)	4 (66.7%), 3 (50.0%)
Homogeneous	30 (46.2%)					21.5 (14.8–20.3)	22 (73.3%), 13 (43.3%)
Heterogeneous	29 (44.6%)					18.0 (15.8–20.2)	26 (89.7%), 10 (34.5%)
Nonperipheral “washout”		0.034	.85	0.011	.92		
Absent	15 (23.1%)					22.0 (13.2–21.6)	11 (73.3%), 7 (46.7%)
Present	50 (76.9%)					19.0 (16.0–19.7)	41 (82.0%), 19 (38.0%)
Enhancing “capsule”		3485	.06	3425	.06		
Absent	19 (29.2%)					24.0 (18.1–23.7)	17 (89.5%), 12 (63.2%)
Present	46 (70.8%)					16.5 (14.5–18.4)	35 (76.1%), 14 (30.4%)
Continuity of an enhancing “capsule”		6.379	.041	8.918	.012		
Absent	19 (29.2%)					24.0 (18.1–23.7)	17 (89.5%), 12 (63.2%)
Discontinuous	31 (47.7%)					17.0 (15.7–19.5)	27 (87.1%), 9 (29.0%)
Continuous	15 (23.1%)					13.0 (9.12–18.88)	8 (53.3%), 5 (33.3%)

Note–Survival times were analyzed using a univariate log-rank test. Furthermore, the log-rank test was weighted toward earlier events by assessment within the first 24 months after treatment and using the Gehan-Breslow-Wilcoxon test. When evaluating PFS for the first 2 years by imaging features, patients with 1, 2, and 3 tumors survived a median of 22.0 months (95% CI, 16.8–20.5), 15.0 months (95% CI, 12.1–20.6), and 10.5 months (95% CI, 0.2–20.8), respectively. The 1-year and 2-year rates for patients with 1 tumor were 83.7% and 46.9%, respectively, those for patients with 2 tumors were 75.0% and 25.0%, respectively, and those for patients with 3 tumors were 50.0% and 0, respectively.

APHE = arterial phase hyperenhancement; CI = confidence interval; PFS = progression-free survival.